Journal of Materials Chemistry A

Accepted Manuscript

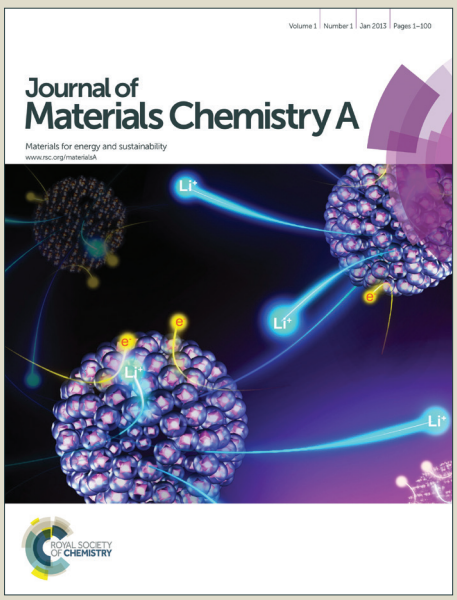

ROYAL SOCIETY OF CHEMISTRY

www.rsc.org/materialsA

Journal of Materials Chemistry A

ARTICLE

WSe_2 and $W(Se_xS_{1-x})_2$ nanoflakes grown on carbon nanofibers for the electrocatalytic hydrogen evolution reaction

Received 00th January 20xx,
Accepted 00th January 20xx

DOI: 10.1039/x0xx00000x

www.rsc.org/

MeiLing Zou, JiaDong Chen, LongFei Xiao, Han Zhu, TingTing Yang, Ming Zhang, MingLiang Du*

Transition metal dichalcogenides (TMD) have recently attracted substantial attention due to their potential application to the catalysis of the hydrogen evolution reaction (HER). In this study, triangular WSe_2 and $W(Se_xS_{1-x})_2$ nanoflakes uniformly dispersed on the surface of electrospun carbon nanofiber mats were synthesized in a chemical vapor deposition (CVD) system. The morphology and structure of these products were systematically characterized, revealing that WSe_2 nanoflakes are configured in the 2H phase with high crystallinity, and the $W(Se_xS_{1-x})_2$ nanoflakes are configured in the alloy form without any obvious phase separation. The hybrid catalyst mats were directly used as hydrogen evolution cathodes to investigate their HER activity. Excellent HER performances, including low overpotential, high current density and long-term stability, were achieved by optimizing the content of the initial W precursor and the appropriate substitution of selenium with sulfur, which was resulted from the appropriate cover density and thickness of the WSe_2 nanoflakes and the defective structure of the $W(Se_xS_{1-x})_2$ nanoflakes.

Introduction

Sustainable hydrogen production is an essential prerequisite of the future hydrogen economy, and the electrochemical hydrogen evolution reaction (HER) has been suggested as an efficient route to the sustainable production of H_2.[1-4] In recent years, active research has continued to develop non-precious metal-based electrocatalysts for HER, including metal sulfides,[5-7] metal selenides,[8-10] metal boride,[11, 12] metal carbides,[13-15] metal phosphides,[16-18] and heteroatom-doped nanocarbons.[19-21] Among the various candidates, layered transition metals (transition metal dichalcogenides, TMD) are of particular interest. Recently, WSe_2, a typical TMD, was demonstrated as a promising HER catalyst; it has a similar structure to that of MoS_2 in which tungsten atoms are sandwiched between selenium atoms in a hexagonal arrangement by strong covalent bonds, and the neighboring layers are bound by weak van der Waals interactions.[22, 23]

Experimental and computational studies have highlighted that the HER activity of WSe_2 correlates with the number of catalytically active sites.[24, 25] Many studies have also suggested that the exposed edges or defects serve as the catalytically active sites.[26, 27] Therefore, the ability to control the synthesis of nanosized WSe_2 with an abundant amount of edge sites or defects is an effective strategy to obtain an efficient WSe_2 HER electrocatalyst. For example, vertically aligned WSe_2 with preferentially exposed active edge sites was obtained through selenization of a W thin film magnetron sputtered on an Si substrate or carbon fiber paper, which improved the HER performance.[26] In our recent investigation, we also demonstrated that 3D dendritic WSe_2 on carbon nanofibers with a high fraction of exposed active edge sites is a highly efficient electrocatalyst for HER.[28] In addition to structural engineering, another process to tune the HER activity of TMD can be realized by tailoring their chemical composition. Generally, the incorporation of transition metals, such as Co, Ni, and Fe, into TMD can enhance their catalytic activity for HER.[29-31] Furthermore, partial or full substitution of chalcogens into TMD by other chalcogens has led to satisfactory HER performance.[27, 32, 33] For example, the introduction of selenium to substitute for sulfur in MoS_2 continuously modulates the d-band electronic structure of molybdenum, resulting in tuned hydrogen adsorption free energy, as well as electrocatalytic activity.[32]

Motivated by the success of WSe_2 nanostructures synthesized by chemical vapor deposition (CVD), the present study investigated the growth of WSe_2 nanoflakes and the substitution of selenium with sulfur in WSe_2 to modify its physical and chemical properties. Many experimental studies have suggested that the conductivity of TMD with electrolyte is also indispensable for excellent HER performance.[34-36] Among the various substrates for HER catalysts, electrospun carbon nanofiber mats (CFM) prepared from electrospun polyacrylonitrile nanofiber mats (PAN FM) after thermal treatments are promising candidates with a large specific

Key Laboratory of Advanced Textile Materials and Manufacturing Technology of the Ministry of Education, College of Materials and Textiles, Zhejiang Sci-Tech University, 310018, P. R. China

Electronic Supplementary Information (ESI) available: Schematic for the set-up used for the growth of $W(Se_xS_{1-x})_2$ nanoflakes on CFM; SEM images of WO_3-C-10; cross-sectional SEM images of the synthesized catalysts; SEM images of WSe_2-C-y to detect the thickness of the WSe_2 nanoflakes; element maps of $W(Se_{0.4}S_{0.6})_2$-C-10; EELS spectra; digital photograph of the catalyst mat; CV plots of the catalytic electrodes; Impedance spectra; representative SEM images of the electrodes after chronoamperometric response test for 12h; The movie of bubble release. See DOI: 10.1039/x0xx00000x

surface area and favorable high conductivity.[37] Synthesizing WSe_2 or $W(Se_xS_{1-x})_2$ alloy nanoflakes on CFM exploits the merits of CFM and avoids the usage of a polymer binder to immobilize the catalyst on the electrode surfaces, which will benefit the practical application of the catalysts.

In this study, we present the design and fabrication of WSe_2 and $W(Se_xS_{1-x})_2$ alloy nanoflakes on flexible CFM ($W(Se_xS_{1-x})_2$-C-y, where x is the atom fraction of chalcogen, and y is the initial mass fraction of the W precursor in PAN powder) via a CVD method. First, WO_3 nanoparticles (WO_3 NPs) were thermally decomposed from $(NH_4)_6H_2W_{12}O_{40}$ contained in the electrospun PAN FM precursor. Subsequently, WSe_2 or $W(Se_xS_{1-x})_2$ alloy nanoflakes were synthesized through CVD (Figure S1). In this process, the temperature gradient of the furnace was used to synthesize $W(Se_xS_{1-x})_2$-C-y, which has been successfully used in previous studies to grow compositionally tunable chalcogenide alloy nanoflakes.[38, 39] The loading amount of WSe_2 nanoflakes on CFM was tuned by adjusting the initial W precursor in the electrospun PAN FM substrate, and the substitution of selenium with sulfur was realized using selenium along with sulfur powder as the reductants. $W(Se_xS_{1-x})_2$-C-y directly served as the working electrodes in a three-electrode system and exhibited excellent electrocatalytic properties for HER, displaying a relatively low overpotential, small Tafel slope, high exchange current density and good stability.

Experimental

Ammonium metatungstate hydrate contained PAN FM (W-PAN FM) was prepared via electrospinning following a previous method.[28] The WSe_2 or $W(Se_xS_{1-x})_2$ nanoflakes on the CFM were synthesized through CVD. First, W-PAN FM was cut into suitable flat pieces, placed on an alumina boat, and then moved into the middle of the heating zone of a slender quartz tube for heat treatments. The furnace was heated to 280 °C from room temperature and was maintained at this temperature for 6 h for the sufficient pre-oxidation of the PAN nanofibers, as well as the thermal decomposition of $(NH_4)_6H_2W_{12}O_{40}$ to form uniformly dispersed WO_3 NPs. Subsequently, a boat loaded with 5 mmol of Se (or 2.5 mmol S + 2.5 mmol Se) powder was placed upstream at a distance of approximately 20 cm from the center of the furnace (Figure S1). Prior to heating to higher temperatures, an Ar flow was introduced into the system at a rate of 150 sccm for 20 min to ensure favorable conditions for the sample synthesis. The furnace was then ramped to 1000 °C at 5 °C min^{-1} and was maintained at this temperature for another 6 h to sufficiently reduce the WO_3 NPs inside of the PAN nanofibers and to completely graphitize the PAN nanofibers. During this time, the pressure inside of the tube and the flow rate of Ar were maintained at 1 Torr and 150 sccm, respectively. After the treatment, the temperature was allowed to return to room temperature.

Characterizations

The morphology of the prepared samples was observed on a JSM-6700F FE-SEM (JEOL, Japan) at an acceleration voltage of 3 kV. Transmission electron microscopy (TEM) and scanning transmission electron microscopy (STEM) were performed using a transmission electron microscope (Tecnai G2 F30 S-Twin, Philips-FEI) at an acceleration voltage of 300 kV. X-ray diffraction (XRD) patterns of the hybrid films were obtained on a diffractometer (Bruker AXS D8) using Cu K_α radiation (k = 0.15418) with a 2θ scan from 5 to 80 degrees at a step of 0.02. X-ray photoelectron spectra of the samples were recorded using an X-ray photoelectron spectrometer (Kratos Axis Ultra DLD) with an aluminum (mono) K_α source (1486.6 eV). Raman spectra were recorded using a Renishaw inVia Raman microscope with a 532 nm laser excitation source.

Electrochemical Measurements

The HER performances of the as-grown catalysts were tested in 0.5 M H_2SO_4 (aq) electrolyte (deaerated by N_2). The catalysts mats were cut into 1 × 1 cm^{-2} pieces, fixed in a Teflon electrode clamp, and used as the working electrode. A Pt mesh and a saturated calomel electrode (E(RHE) = E(SCE) + 0.244 V) were used as the counter and reference electrodes, respectively. Cyclic voltammograms (CVs) were obtained for 400 cycles to bubble away the surface contaminates and simultaneously stabilize the catalysts. The potential values were plotted with reference to the standard reversible hydrogen electrode (RHE), and the current measurements were normalized to the geometric area of the tested samples. The performance of the hydrogen evolution catalysts was measured using linear sweep voltammetry beginning at +0.3 V and ending at −0.50 V vs RHE with a scan rate of 2 mV s^{-1}. Electrochemical impedance spectroscopy (EIS) was performed when the working electrode was biased at a constant value of −0.15 V vs RHE while sweeping a frequency from 5 MHz to 10 mHz. A chronoamperometric response was required under a static overpotential of −0.2 V vs RHE. All electrochemical studies were performed on a CHI660E workstation (Shanghai Chenhua, Shanghai) in a three-electrode configuration.

Results and discussion

In this study, there were four major steps involved in the detailed growth of WSe_2 nanoflakes on CFM: (1) the thermal decomposition of $(NH_4)_6H_2W_{12}O_{40}$ contained in the PAN nanofibers to create uniformly dispersed WO_3 NPs (Figure S2), (2) the sublimation and transport of Se vapor by a forced flow of Ar carrier gas, (3) the diffusion of Se vapor from the gas phase onto WO_3 NPs contained on the CFM substrate to reduce the surface WO_3 NPs on the CFM to form volatile suboxides WO_{3-x}, and (4) the rapid selenization of WO_{3-x} NPs into WSe_2 species for the lateral growth or incorporation of WSe_2 nanoflakes on CFM. Because selenium is highly reactive at high temperatures, the WO_3 NPs inside of the carbon nanofibers are activated by the selenium vapor and transform gradually to the outside surface of the CFM to participate in further selenization and growth. As shown in Figure 1, triangular WSe_2 nanoflakes were synthesized on CFM with various coverages using a simple CVD method. The CFM consisting of carbon nanofibers 0.2~0.3 μm in diameter is a three-dimensional substrate after thermal treatments. Figure 1a-c presents the SEM images of WSe_2-C-10, WSe_2-C-20 and WSe_2-C-30, respectively. In previous reports, WSe_2 was

typically only deposited onto the surface of the substrate, such as Si substrates or carbon fiber paper. However, in the present investigation, WSe_2 nanoflakes with triangular morphologies are dispersed uniformly onto the surface of nearly each carbon nanofiber of the three-dimensional CFM (Figure S3), and high HER activity of the catalysts was anticipated due to the high specific area of the CFM and the abundant number of exposed edges of WSe_2.

A typical TEM image of a representative sample (WSe_2-C-10) shows that the obtained WSe_2 nanostructures are bent triangular nanoflakes with edge lengths of 200-500 nm (Figure 1d) on the surface of the carbon nanofibers. Figure 1e shows the high-resolution transmission electron microscopy (HRTEM) image of a typical nanoflake that demonstrates the single-crystalline nature of the 2D structure with a lattice spacing of 2.8 Å, in agreement with the (100) plane of WSe_2. Elemental mapping on the WSe_2-C-10 sample shows the uniform chemical composition throughout the material (Figure 1f). The differences in the thicknesses of the WSe_2 nanoflakes among these three samples (Figure S4) were also revealed by TEM studies, and the thickness of the WSe_2 nanoflakes increased by increasing the W precursor in the carbon nanofibers. Most of these WSe_2-C-10 triangular nanoflakes have 6-8 layers, whereas WSe_2-C-30 has as many as 15 layers. The differences in thickness of the WSe_2 nanoflakes may result in significant changes in the electrocatalytic activity of the catalysts, which is discussed later.

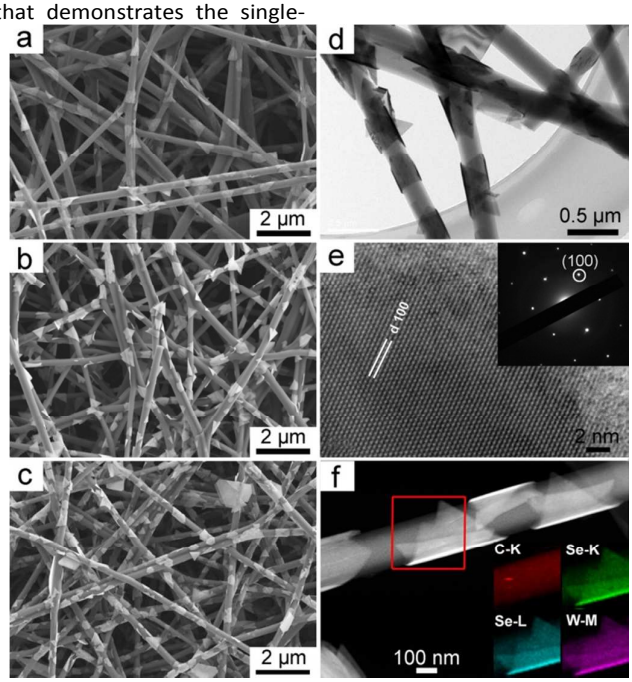

Figure 1. SEM images of (a) WSe_2-C-10, (b) WSe_2-C-20 and (c) WSe_2-C-30; (d) low-magnification TEM image of WSe_2-C-10; (e) HRTEM image of a WSe_2 nanosheet of WSe_2-C-10; (f) high-angle annular dark field (HAADF) STEM image of WSe_2-C-10; inset contains the element maps obtained from the mapping area in image f.

The incorporation of other chalcogens into WS_2 and MoS_2 will enhance their catalytic activity for HER.[32, 33] For WSe_2, the hydrogen binding energy at the selenide W-edge is too weak (ΔG_H = 170 mV), and theoretical calculations suggest that the substitution of an appropriate portion of selenium by sulfur may help attain a ΔG_H value more close to thermoneutral, leading to improved HER activity.[24] Inspired by this strategy, we synthesized $W(Se_xS_{1-x})_2$ alloy nanoflakes on CFM and explored their influence on the spectroscopic properties and electrochemical activities of the material. PAN FM containing 10 and 20% $(NH_4)_6H_2W_{12}O_{40}$ was selected as the representative precursor, and Figures 2a and b present the SEM images of the final products, respectively. Bent triangular nanoflakes were dispersed uniformly on the surface of each carbon nanofiber (Figure S2). The edge lengths of the second sample were approximately two times longer than the lengths of the first sample. TEM combined with energy-dispersive X-ray spectroscopy (EDS) was used to investigate the microstructure and elemental composition of these nanoflakes (Table S1). Figure 2c shows the typical TEM image of the first sample, and the inset in Figure 2c shows the HRTEM image of the alloy nanoflake with a honeycomb-like structure. The EDS spectrum shown in Figure 1d demonstrates that the nanoflakes consist of W, S, and Se elements with an Se mole fraction [x, Se/(S+Se)] of ~0.4, indicating the composition of the nanoflake as $W(Se_{0.4}S_{0.6})_2$, denoted as sample $W(Se_{0.4}S_{0.6})_2$-C-10. Analogously, the second sample was denoted as $W(Se_{0.2}S_{0.8})_2$-C-20. Note that the increase in the W precursor facilitates the substitution of selenium with sulfur, leading to an increased S mole fraction in the alloy nanoflakes. This observation is reasonable because S is more active than Se at high temperatures, and a faster substitution and growth of the alloy nanoflakes is subsequently promoted, resulting in an increased lateral dimension and decreased Se mole fraction in the alloy nanoflakes. The increased edge lengths would cause decreases in the density of active edge sites, and finally affect the HER activity.[40]

EDS element mapping was applied to investigate the spatial distribution of constituent elements within the $W(Se_xS_{1-x})_2$ alloys (Figure S5), confirming the homogeneous distribution of W, Se and S elements across the entire substrate. Furthermore, the representative high-resolution element images of $W(Se_{0.4}S_{0.6})_2$-C-10 obtained from STEM are shown in Figures 2e and f. W, Se and S show high spatial correlation over the examined area, suggesting a single-phase construction of nanoscale S and Se with no phase separation of WSe_2 and WS_2. Moreover, line-scan electron energy loss spectroscopy (EELS) from the indicated position revealed that the signal intensity of each element changed consistently with the thickness of the alloy nanoflakes (Figure S6). Further insight into the morphology of the alloy nanoflakes revealed many dislocations and distortions compared with single-component WSe_2 nanoflakes (Figure 3). As indicated in many previous studies, these defects typically serve as active sites and can crack the crystal to expose specific crystal planes, subsequently increasing the accessible internal surface area, which may dramatically improve the electrocatalytic HER performance.[27, 40]

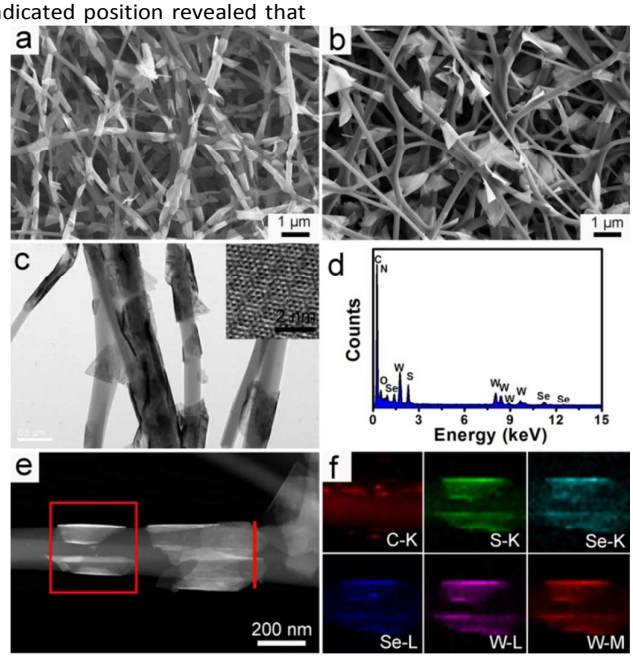

Figure 2. SEM images of (a) $W(Se_{0.4}S_{0.6})_2$-C-10 and (b) $W(Se_{0.2}S_{0.8})_2$-C-20; (c) low-magnification TEM image of $W(Se_{0.4}S_{0.6})_2$-C-10; inset is the HRTEM of the $W(Se_{0.4}S_{0.6})_2$ nanoflake; (d) EDS spectrum from the region in image c; (e) HAADF STEM image of $W(Se_{0.4}S_{0.6})_2$-C-10; (f) corresponding element maps obtained from the mapping area in image e.

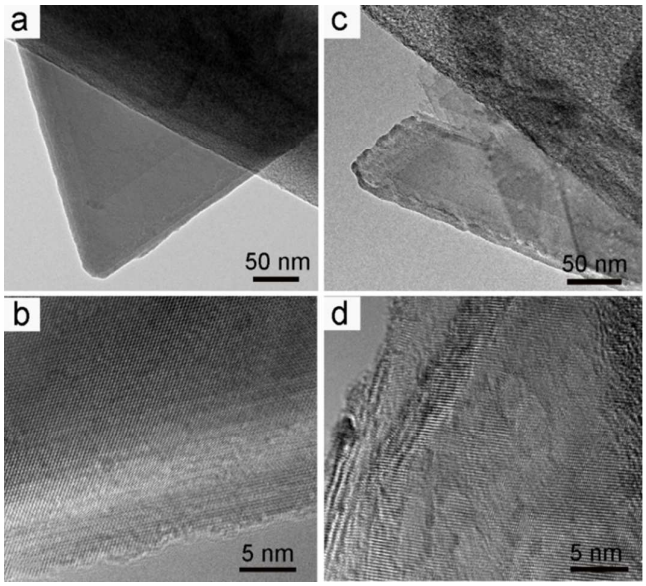

Figure 3. TEM images of (a and b) WSe_2-C-10 and (c and d) $W(Se_{0.4}S_{0.6})_2$-C-10.

Journal of Materials Chemistry A

ARTICLE

The structural information of the products was investigated by XRD and Raman analysis. As shown in Figure 4a, all of the diffraction peaks in the XRD patterns can be assigned to hexagonal 2H-tungsten dichalcogenide (JCPDS card No. 38-1388), revealing the high purity of the products. The good crystallinity of all of these samples may benefit their electrochemical stability in acidic electrolytes. Moreover, the substitution of selenium by sulfur leads to an upshift of all of the main diffraction peaks, which further implies their mixing at the atomic level.[32] As shown in Figure 4b, two broad peaks at 1200-1600 cm^{-2} of all five samples are ascribed to the D and G bands of the carbon nanofiber substrate. Only one prominent peak in the WSe_2-C-y samples is distinctly observed below 1000 cm^{-2}, where the A_{1g} and E_{2g} peaks of WSe_2 are expected because these two modes are closely located at 253 and 250 cm^{-2}, respectively.[26] With the introduction of sulfur, these vibrational modes shift to higher frequencies, suggesting that the interaction between sulfur and selenium atoms enhances the related W-Se modes and increases their vibrational frequencies. Meanwhile, two pronounced peaks assigned to the 2H WS_2-like E_{2g} (351.9 cm^{-2}) and A_{1g} (415.8 cm^{-2}) modes emerge. Compared with the respective E_{2g} and A_{1g} peaks at 353.6 and 418.4 cm^{-1} of pure WS_2 nanoflakes, the blue-shift of these two peaks is diagnostic of typical $W(Se_xS_{1-x})_2$ alloys.[32]

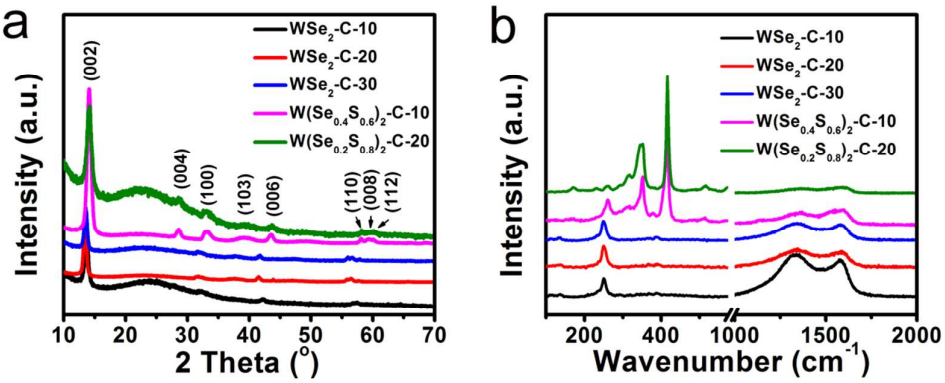

Figure 4. Spectroscopic characterizations of various samples: (a) XRD, (b) Raman.

We also investigated the chemical states of tungsten and chalcogen in WSe_2 and $W(Se_xS_{1-x})_2$ alloys using XPS analysis. Figure 5a-c illustrates the W 4f, Se 3d and S 2p high-resolution spectra of these samples. In Figure 5a, the two obvious peaks at 32.6 and 34.7 eV in the WSe_2-C-y samples are the characteristic peaks of W $4f_{7/2}$ and W $4f_{5/2}$, respectively. The substitution of selenium causes a small shift in these peaks to higher binding energies, which agrees with previously reported values for the WSe_2 and WS_2 systems.[32] Similar changes can also be observed in the Se 3d and S 2p XPS spectra. The peaks at approximately 54.5 and 55.4 eV are attributed to the Se $3d_{5/2}$ and Se $3d_{3/2}$ binding energies, respectively, as shown in Figure 5b. Meanwhile, with increasing sulfur content, the peaks of selenium shift to higher binding energies. Note that with an increasing S concentration from 0.6 to 0.8, the S $2p_{3/2}$ and S $2p_{1/2}$ peaks of the alloy nanoflakes appear to be dominant with a slight downshift compared with bulk WS_2.[6]

Based on the above discussion, WSe_2 and $W(Se_xS_{1-x})_2$ with bent triangular morphologies were successfully prepared on the surface of electrospun carbon nanofibers. All of the resulting nanoflakes were rich in exposed edges, which is critical to HER electrocatalysis. The cover density of WSe_2 can be adjusted by varying the initial $(NH_4)_6H_2W_{12}O_{40}$ precursor in the electrospun PAN nanofibers. Increasing the W precursor will lead to increased thickness of the WSe_2 nanoflakes. In addition, using a simple method, we successfully synthesized $W(Se_xS_{1-x})_2$ alloy nanoflakes with an abundant amount of defects on the carbon nanofibers. Due to the higher activity of S over Se at high temperatures, increasing the W precursor decreases the Se/S ratio and greatly increases the edge length of the alloy nanoflakes.

Journal of Materials Chemistry A

ARTICLE

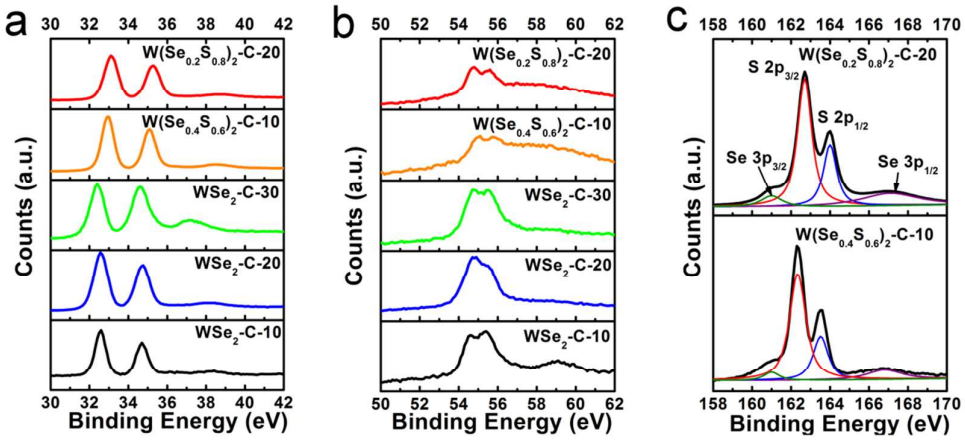

Figure 5. (a-c) High-resolution XPS spectra of W 4f, Se 3d and S 2p of various samples, respectively.

The HER catalytic activity of WSe_2 and $W(Se_xS_{1-x})_2$ nanoflakes on carbon nanofibers was evaluated in 0.5 M H_2SO_4 with a typical three-electrode electrochemical cell setup. Because these various catalysts were directly assembled as the working electrode in HER, the catalyst thickness was taken into consideration. The cross-sectional images of these catalysts were recorded, as shown in Figure S3 a-j, indicating the comparable thickness of each sample and the homogenous distribution of the WSe_2 (or $W(Se_xS_{1-x})_2$) nanosheets throughout the hybrid catalysts. Generally, electrospin-derived neat CFM are brittle, whereas these hybrid catalysts are flexible (Figure S7), which may be due to the high density of flexible WSe_2 nanoflakes alongside the carbon nanofiber backbone, as well as the suitable thickness of these catalyst mats.

Figure 6a shows the polarization curves of the final products normalized to the geometric area of the electrode. CFM and WSe_2 NPs show negligible activity, whereas $W(Se_xS_{1-x})_2$-C-y samples exhibit robust HER activity with small onset potentials over the range of 80-110 mV and with the cathodic current increasing rapidly under more negative potentials. Interestingly, WSe_2-C-20 demonstrates the best catalytic activity with an overpotential (η) of 158 mV at a current density of 10 mA cm^{-2} (Table 1), in contrast to other samples, such as WSe_2-C-10 (213 mV) and WSe_2-C-30 (188 mV). This exceptional HER activity is further illustrated by comparing the Tafel slopes of WSe_2-C-20 (98 mV dec^{-1}) with other samples (Figure 6b and Table 1). For WSe_2-C-y samples, WSe_2-C-30 has the highest cover density of the WSe_2 nanoflakes, and its HER performance is better than that of WSe_2-C-10 but is inferior to that of WSe_2-C-20. Previous reports have indicated that the HER efficiency is related to the thickness of TMD because the high interlayer potential barrier may result in a lower interlayer electron hopping efficiency, consequently reducing the HER activity.[41] We can conclude that the increased thickness of the WSe_2 nanoflakes in WSe_2-C-30 (Figure S4) is a major cause for its reduced catalytic activity, suggesting that the thickness and cover density of WSe_2 nanoflakes can be optimized to balance the catalytic activity. With the substitution of selenium by sulfur, $W(Se_{0.4}S_{0.6})_2$-C-10 and $W(Se_{0.2}S_{0.8})_2$-C-20 showed a greatly improved HER efficiency over WSe_2-C-10 and WSe_2-C-30 that was slightly inferior to WSe_2-C-20 (Figure 6a and b). The overpotential to achieve an electrocatalytic current density of 10 mA cm^{-2} for $W(Se_{0.4}S_{0.6})_2$-C-10 and $W(Se_{0.2}S_{0.8})_2$-C-20 is 174 and 178 mV, respectively. One major cause for the good catalytic behavior of these two samples may be the unique defect-rich alloy nanoflakes, which impart additional active edge sites (Figure 3). Moreover, the band gap of $W(Se_{0.4}S_{0.6})_2$ and $W(Se_{0.2}S_{0.8})_2$ is approximately 1.69 and 1.65 eV, respectively, and slightly larger than bulk WSe_2 with bind gap of 1.6 eV.[42] However, the substitution of selenium with sulfur atoms lead to lower Tafel slopes, which is probably afforded by the much increased active edge sites of the alloy nanoflakes. The $W(Se_{0.4}S_{0.6})_2$-C-10 exhibited a better HER performance than $W(Se_{0.2}S_{0.8})_2$-C-20, which could result from the markedly longer edge length of $W(Se_{0.2}S_{0.8})_2$ that reduces the density of the active sites. We also synthesized WS_2-C-20 as a control. The SEM image and the polarization curve can be seen in Figure S8. The edge length of WS_2 is comparable to $W(Se_{0.2}S_{0.8})_2$ and much larger than WSe_2, which can be resulted from the much activity nature of S than Se at high temperature that accelerated the reduction of WO_3 NPs and the growth of WS_2 nanosheets. The onset potential of WS_2-C-20 is about −200 mV and larger than that of $W(Se_{0.2}S_{0.8})_2$-C-20, indicating the favorable adsorption of H_{ads} on the S substituted edge.

We also estimated the relative difference in electrochemically active surface areas among these electrodes using a simple cyclic voltammetry (CV) method. The electrostatic capacities of these electrodes under 0-0.8 V vs

RHE at a scan rate of 0.1 V s^{-1} were recorded (Figure S8 a). Typically, the exchange current density (j_0) is expected to be proportional to the catalytically active surface area. The j_0 values of these electrodes calculated from the Tafel plots in Figure 6b are summarized in Table 1. An alternative approach to estimate the effective surface area is to measure the capacitance of the double layer (C_{dl});[8] thus, CV plots under a potential range (0.1-0.2 V vs RHE) in which no faradic current was observed at various scan rates (0.5-5 mV s^{-1}) were recorded (Figure S9 b-f). Subsequently, the C_{dl} of these electrodes were collected and are shown in Figure 6c and Table 1. The electrochemical effective surface areas of WSe_2-C-20 (430 mF cm^{-2}), WSe_2-C-30 (313 mF cm^{-2}) and $W(Se_xS_{1-x})_2$-C-10 (376 mF cm^{-2}) are approximately 1.78, 1.3 and 1.56 times larger than WSe_2-C-10 (241 mF cm^{-2}), respectively. This increase in electrochemically active surface area demonstrates the proliferation of active sites, which improves the catalytic performance. Impedance measurements were performed at η = 150 mV (Figure S10), and the charge transfer resistances of these electrodes vary in a trend that agrees with the CV results. At a potential below the onset potential during the test, many bubbles are generated on the electrode surface (see Movie S1 of the $W(Se_xS_{1-x})_2$-C-10 electrode at a constant potential of –0.4 V vs RHE as an example). These bubbles are easily released from the CFM surface, which is a highly desirable property for the practical application of HER catalysts. To evaluate the catalyst durability in acidic environments, potentiostatic electrolysis cycling was performed at –0.2 V vs RHE for 12 h. As shown in Figure 6d, the current densities of these electrodes remained stable for 12 h, and the slight decrease in current density could be ascribed to the continuously released bubbles generated from the surface of the CFM and to the consumption of H^+ during the tests. The representative SEM images of these electrodes after the 12 h cycling test are given in Figure S11, showing no obvious changes in morphology. This excellent durability shows promise for practical long-term applications of the catalysts. The comparison of some state-of-the-art WS_2 and WSe_2 HER electrocatalysts was summarized in Table S2, revealing the excellent HER performance of the electrodes synthesized in this study.

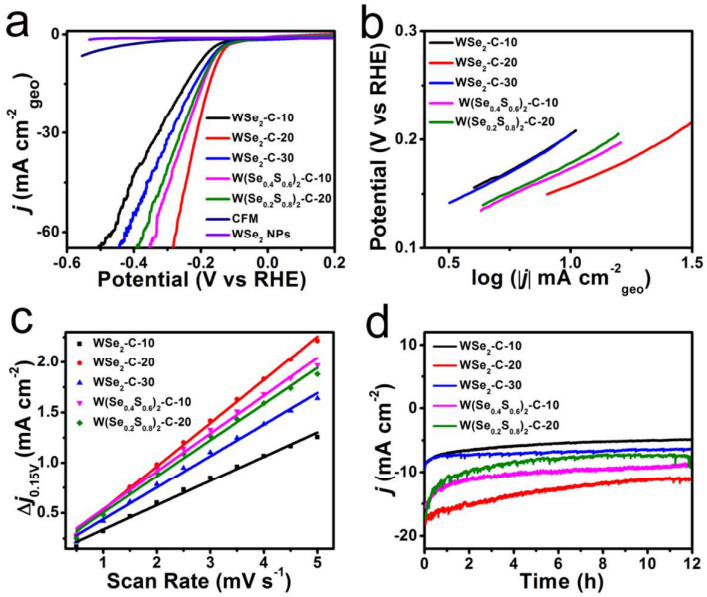

Figure 6. (a) Polarization curves obtained for several electrodes as indicated; (b) corresponding Tafel plots; (c) linear fitting of the capacitive currents of the catalysts vs scan rates; (d) time dependence of current density under a static overpotential of −0.2 V vs RHE.

Table 1. Electrocatalytic performance of the five different catalysts.

	WSe_2-C-10	WSe_2-C-20	WSe_2-C-30	$W(Se_{0.4}S_{0.6})_2$-C-10	$W(Se_{0.2}S_{0.8})_2$-C-20
η @ j = 10 mA cm^{-2} (mV)	213	158	188	174	178
Tafel slope (mV dec^{-1})	117	98	116	106	106
j_0 (mA cm^{-2})	0.195	0.240	0.204	0.229	0.214
C_{dl} (mF cm^{-2})	241	430	313	376	359

Conclusions

Triangular WSe_2 and $W(Se_xS_{1-x})_2$ nanoflakes with an abundant amount of exposed edges uniformly dispersed on the surface of conductive electrospun CFM were synthesized in a CVD system. The cover density of WSe_2 nanoflakes can be easily controlled by adjusting the initial W precursor, while the thickness of the nanoflakes increases with the increasing W precursor. $W(Se_xS_{1-x})_2$ nanoflakes with no obvious phase separation were also synthesized, and the partial substitution

of selenium with sulfur makes the basal planes of the $W(Se_xS_{1-x})_2$ nanoflakes substantially more defective than the WSe_2 nanoflakes. The products were directly used as hydrogen evolution cathodes to highlight the merits of these catalysts. All of these electrodes exhibited low overpotential, high exchange current density, and long-tern stability for HER. More importantly, the excellent HER performance can be obtained either by adjusting the suitable cover density and thickness of the WSe_2 nanoflakes or by optimizing the substitution of selenium with sulfur. The present study provides a simple method for the synthesis of CFM-based TMD, which may have promising applications in other fields.

Acknowledgements

This study was supported by the National Natural Science Foundation of China (NSFC) (Grant no. 51373154), Program for Innovative Research Team of Zhejiang Sci-Tech University and the 521 Talent Project of Zhejiang Sci-Tech University.

Notes and references

1 X. Zou and Y. Zhang, *Chem. Soc. Rev.*, 2015, DOI: 10.1039/C4CS00448E.
2 C. G. Morales-Guio, L. A. Stern and X. Hu, *Chem. Soc. Rev.*, 2014, **43**, 6555-6569.
3 H. H. Li, C. H. Cui, S. Zhao, H. B. Yao, M. R. Gao, F. J. Fan and S. H. Yu, *Adv. Energy Mater.*, 2012, **2**, 1182-1187.
4 C. Wang, M. Chi, G. Wang, D. van der Vliet, D. Li, K. More, H. H. Wang, J. A. Schlueter, N. M. Markovic and V. R. Stamenkovic, *Adv. Funct. Mater.*, 2011, **21**, 147-152.
5 X. Zheng, J. Xu, K. Yan, H. Wang, Z. Wang and S. Yang, *Chem. Mater.*, 2014, **26**, 2344-2353.
6 M. A. Lukowski, A. S. Daniel, C. R. English, F. Meng, A. Forticaux, R. J. Hamers and S. Jin, *Energy Environ. Sci.*, 2014, **7**, 2608-2613.
7 C. Y. Lin, D. Mersch, D. A. Jefferson and E. Reisner, *Chem. Sci*, 2014, **5**, 4906-4913.
8 D. Kong, H. Wang, Z. Lu and Y. Cui, *J. Am. Chem. Soc.*, 2014, **136**, 4897-4900.
9 M. R. Gao, Z. Y. Lin, T. T. Zhuang, J. Jiang, Y. F. Xu, Y. R. Zheng and S. H. Yu, *J. Mater. Chem.*, 2012, **22**, 13662-13668.
10 F. H. Saadi, A. I. Carim, J. M. Velazquez, J. H. Baricuatro, C. C. L. McCrory, M. P. Soriaga and N. S. Lewis, *ACS Catal.*, 2014, **4**, 2866-2873.
11 M. D. Scanlon, X. Bian, H. Vrubel, V. Amstutz, K. Schenk, X. Hu, B. Liu and H. H. Girault, *Phys. Chem. Chem. Phys.*, 2013, **15**, 2847-2857.
12 H. Vrubel and X. Hu, *Angew. Chem.*, 2012, **51**, 12703-12706.
13 X. Fan, H. Zhou and X. Guo, *ACS Nano*, 2015, **9**, 5125-5134.
14 K. Zhang, Y. Zhao, S. Zhang, H. Yu, Y. Chen, P. Gao and C. Zhu, *J. Mater. Chem. A*, 2014, **2**, 18715-18719.
15 C. Wan, Y. N. Regmi and B. M. Leonard, *Angew. Chem.*, 2014, **53**, 6407-6410.
16 J. Tian, Q. Liu, A. M. Asiri and X. Sun, *J. Am. Chem. Soc.*, 2014, **136**, 7587-7590.
17 T. Wang, K. Du, W. Liu, Z. Zhu, Y. Shao and M. Li, *J. Mater. Chem. A*, 2015, **3**, 4368-4373.
18 P. Jiang, Q. Liu and X. Sun, *Nanoscale*, 2014, **6**, 13440-13445.
19 I. Y. Jeon, D. Yu, S. Y. Bae, H. J. Choi, D. W. Chang, L. Dai and J. B. Baek, *Chem. Mater.*, 2011, **23**, 3987-3992.
20 Y. Hou, Z. H. Wen, S. M. Cui, S. Q. Ci, S. Mao and J. H. Chen, *Adv. Funct. Mater.*, 2015, **25**, 872-882.
21 S. Gao, G. D. Li, Y. Liu, H. Chen, L. L. Feng, Y. Wang, M. Yang, D. Wang, S. Wang and X. Zou, *Nanoscale*, 2015, **7**, 2306-2316.
22 A. Y. S. Eng, A. Ambrosi, Z. Sofer, P. Šimek and M. Pumera, *ACS Nano*, 2014, **8**, 12185-12198.
23 J. M. Velazquez, F. H. Saadi, A. P. Pieterick, J. M. Spurgeon, M. P. Soriaga, B. S. Brunschwig and N. S. Lewis, *J. Electroanal. Chem.*, 2014, **716**, 45-48.
24 C. Tsai, K. Chan, F. Abild-Pedersen and J. K. Norskov, *Phys. Chem. Chem. Phys.*, 2014, **16**, 13156-13164.
25 T. F. Jaramillo, K. P. Jørgensen, J. Bonde, J. H. Nielsen, S. Horch and I. Chorkendorff, *Science*, 2007, **317**, 100-102.
26 H. Wang, D. Kong, P. Johanes, J. J. Cha, G. Zheng, K. Yan, N. Liu and Y. Cui, *Nano Lett.*, 2013, **13**, 3426-3433.
27 K. Xu, F. Wang, Z. Wang, X. Zhan, Q. Wang, Z. Cheng, M. Safdar and J. He, *ACS Nano*, 2014, **8**, 8468-8476.
28 M. L. Zou, J. F. Zhang, H. Zhu, M. L. Du, Q. F. Wang, M. Zhang and X. W. Zhang, *J. Mater. Chem. A*, 2015, **3**, 12149-12153.
29 D. Merki, H. Vrubel, L. Rovelli, S. Fierro and X. Hu, *Chem. Sci.*, 2012, **3**, 2515-2525.
30 X. J. Lv, G. W. She, S. X. Zhou and Y. M. Li, *RSC Adv.*, 2013, **3**, 21231-21236.
31 J. Li, W. Tang, H. Yang, Z. Dong, J. Huang, S. Li, J. Wang, J. Jin and J. Ma, *RSC Adv.*, 2014, **4**, 1988-1995.
32 Q. Gong, L. Cheng, C. Liu, M. Zhang, Q. Feng, H. Ye, M. Zeng, L. Xie, Z. Liu and Y. Li, *ACS Catal.*, 2015, **5**, 2213-2219.
33 V. Kiran, D. Mukherjee, R. N. Jenjeti and S. Sampath, *Nanoscale*, 2014, **6**, 12856-12863.
34 A. J. Smith, Y. H. Chang, K. Raidongia, T. Y. Chen, L. J. Li and J. Huang, *Adv. Energy Mater.*, 2014, **4**. 1400398.
35 H. Wang, Z. Lu, D. Kong, J. Sun, T. M. Hymel and Y. Cui, *ACS Nano*, 2014, **8**, 4940-4947.
36 J. Kim, S. Byun, A. J. Smith, J. Yu and J. Huang, *J. Phys. Chem. Lett.*, 2013, **4**, 1227-1232.
37 H. Zhu, M. Du, M. Zhang, M. Zou, T. Yang, Y. Fu and J. Yao, *J. Mater. Chem. A*, 2014, **2**, 7680-7685.
38 H. Li, X. Duan, X. Wu, X. Zhuang, H. Zhou, Q. Zhang, X. Zhu, W. Hu, P. Ren, P. Guo, L. Ma, X. Fan, X. Wang, J. Xu, A. Pan and X. Duan, *J. Am. Chem. Soc.*, 2014, **136**, 3756-3759.
39 A. Pan, R. Liu, M. Sun and C.-Z. Ning, *J. Am. Chem. Soc.*, 2009, **131**, 9502-9503.
40 J. Xie, H. Zhang, S. Li, R. Wang, X. Sun, M. Zhou, J. Zhou, X. W. Lou and Y. Xie, *Adv. Mater.*, 2013, **25**, 5807-5813.
41 Y. Tan, P. Liu, L. Chen, W. Cong, Y. Ito, J. Han, X. Guo, Z. Tang, T. Fujita, A. Hirata and M. W. Chen, *Adv. Mater.*, 2014, **26**, 8023-8028.
42 Q. Fu, L. Yang, W. H. Wang, A. Han, J. Huang, P. W. Du, Z. Y. Fan, J. Y. Zhang and B. Xiang, *Adv. Mater.* 2015, DOI: 10.1002/adma.201500368.
43 D. Voiry, H. Yamaguchi, J. W. Li, R. Silva, D. C. B. Alves, T. Fujita, M. W. Chen, T. Asefa, V. B. Shenoy, G. Eda and M. Chhowalla, *Nat. Mater.*, 2013, **12**, 850–855.

WSe_2 and $W(Se_xS_{1-x})_2$ nanoflakes grown on carbon nanofibers for the electrocatalytic hydrogen evolution reaction

MeiLing Zou, JiaDong Chen, LongFei Xiao, Han Zhu, TingTing Yang, Ming Zhang, MingLiang Du*

Triangular $W(SexS_{1-x})_2$ nanoflakes uniformly dispersed on the surface of electrospun carbon nanofiber mats were synthesized. The hybrid catalyst mats were directly used as hydrogen evolution cathodes and exhibit excellent HER performances.